Solid Earth Discuss., 7, 2833–2874, 2015
www.solid-earth-discuss.net/7/2833/2015/
doi:10.5194/sed-7-2833-2015

Solid Earth Discussions
Open Access

Post-glacial reactivation of the Bollnäs fault, central Sweden

A. Malehmir[1], M. Andersson[1], S. Mehta[1], B. Brodic[1], R. Munier[2], J. Place[1], G. Maries[1], C. Smith[3], J. Kamm[1], M. Bastani[3], H. Mikko[3], and B. Lund[1]

[1]Uppsala University, Dept. of Earth Sciences, Uppsala, Sweden
[2]SKB, Stockholm, Sweden
[3]Geological Survey of Sweden, Uppsala, Sweden

Received: 10 September 2015 – Accepted: 21 September 2015 – Published: 15 October 2015

Correspondence to: A. Malehmir (alireza.malehmir@geo.uu.se)

Published by Copernicus Publications on behalf of the European Geosciences Union.

Abstract

Glacially induced intraplate faults are conspicuous in Fennoscandia where they reach trace lengths of up to 155 km with estimated magnitudes up to 8 for the associated earthquakes. While they are typically found in northern parts of Fennoscandia, there are a number of published accounts claiming their existence further south in Fennoscandia and even in northern central Europe. This study focuses on a prominent scarp discovered recently in LiDAR (light detection and ranging) imagery hypothesized to be from a post-glacial fault and located about 250 km north of Stockholm near the town of Bollnäs. The Bollnäs scarp strikes approximately north–south for about 12 km. The maximum vertical offset in the sediments across the scarp is 4–5 m with the western block being elevated relative to the eastern block. To investigate potential displacement in the bedrock and identify structures in it that are related to the scarp, we conducted a multidisciplinary geophysical investigation that included gravity and magnetic measurements, high-resolution seismics, radio-magnetotellurics (RMT), electrical resistivity tomography (ERT) and ground penetrating radar (GPR). Results of the investigations suggest a zone of low-velocity and high-conductivity in the bedrock associated also with a magnetic lineament that is offset horizontally about 50 m to the west of the scarp. The top of bedrock is found ~ 10 m below the surface on the eastern side of the scarp while about ~ 20 m below on its western side. This difference is due to the different thicknesses of the overlying sediments, accounting for the surface topography, while the bedrock surface is likely more or less at the same topographic level on both sides of the scarp. This makes an estimation of the bedrock displacement challenging if not impossible with our datasets. To explain this, we suggest that the Bollnäs scarp is likely associated with an earlier deformation zone, within a wide (> 150 m), highly fractured and water-bearing zone that became active as a reverse fault after the latest Weichselian deglaciation.

SED
7, 2833–2874, 2015

1 Introduction

Glacially induced, intraplate faults are conspicuous in northern Fennoscandia (reviewed in Kuivamäki et al., 1998; Lagerbäck and Sundh, 2008; Olesen et al., 2004 and 2013; Lund, 2015). While some of them have trace lengths up to 155 km with estimated magnitudes up to 8 for the associated earthquakes (e.g., Lagerbäck and Sundh, 2008; Arvidsson, 1996; Lindblom et al., 2015), most are shorter or have less surface expression (Fig. 1). Based on the results from a reflection seismic survey, Ahmadi et al. (2015) reported on the Pärvie post-glacial fault in Sweden, which they imaged down to about 8 km depth (see also Juhlin et al., 2010; Juhlin and Lund, 2011; Lindblom et al., 2015). To the best of our knowledge all known post-glacial faults have been reported to be associated with pre-existing structures (e.g., earlier faults or lithological contacts) that have been reactivated (e.g. MuirWood, 1989; Lagerbäck and Sundh, 2008; Brandes et al., 2012) in a stress regime affected by ice loading and unloading (MuirWood, 1989; Wu et al., 1999; Lund, 2015). Some post-glacial faults appear to be splays of major deformation zones while other faults appear to be isolated structures (e.g., Kuivamäki et al., 1998; Dehls et al., 2000; Lagerbäck and Sundh, 2008). Based on LiDAR-derived imagery, Mikko et al. (2015) suggest that glacially induced faults are not, as previously mapped on aerial photographs, confined solely to the northernmost parts of Sweden but are found also in central Sweden (e.g., Smith et al., 2014). Some of these faults are associated with scarps that strike for more than 12 km giving a recognizable expression on the LiDAR-derived imagery. While LiDAR data provide valuable information, it is important that the presence of the fault is ground-truthed, its extent and geometry at depth are unravelled and if possible an estimate of its displacement is given. These together with the surface expression represented by the scarp can then provide information about their origin, displacement mechanism(s) and, if applicable, the earthquake magnitude.

The Bollnäs scarp in central Sweden is visible in LiDAR imagery for ca. 12 km (Fig. 2). It was initially interpreted to be about 8 km long by Smith et al. (2014) how-

SED
7, 2833–2874, 2015

ever with the aid of magnetic data, this study, it is possible o extend the fault to 12 km. Smith et al. (2014) suggested that the scarp results from post-glacial faulting because in the LiDAR imagery it apparently cross cuts multiple units of glacial and post-glacial sediments (Fig. 2). Although trenching across the scarp to about 3 m depth showed faulted glacial and post-glacial sediments, bedrock was not reached. The presence of water-escape structures and an abundance of landslides in the region were interpreted to result from paleo-seismicity associated with fault rupture (Smith et al., 2014). Since this discovery, a few new areas in the central and northern parts of Sweden have been suggested to host small post-glacial faults (Mikko et al., 2015). While speculative, their presence has also been reported in southern Sweden (Mörner 2004, 2011; Jakobsson et al., 2014) and northern central Europe (Brandes et al., 2015). These inferred post-glacial faults are infrequently studied using multidisciplinary geophysical methods and remain elusive if associated with structures in the bedrock.

For long-term seismic hazard assessment, important for e.g. nuclear waste storage, water dams and mine-waste tailings, unravelling the geometry and kinematics of glacially induced faults is essential. The Bollnäs scarp was chosen as an appropriate candidate for detailed investigations. A number of geophysical investigations including high-resolution gravity and magnetic measurements, refraction and reflection seismics, ERT, RMT, GPR and differential-GPS (DGPS) surveying was carried out. Our objectives were (1) to provide information about the depth to the sediment-bedrock contact on both sides of the scarp, in order to infer potential bedrock displacement and potential related earthquake magnitude, (2) to determine if the scarp was associated with any clear structure within the bedrock and (3) to provide plausible scenarios that can explain how the scarp was formed.

2 Geological background

Smith et al. (2014) provided a detailed description of the post-glacial depositional environment of the Bollnäs area. For completeness, a short summary of their findings

SED
7, 2833–2874, 2015

is provided here. The bedrock (Fig. 3) is dominantly metagranite and gneiss of Svecokarelian age (1.97–1.87 Ga; Sukotjo and Sträng, 2005; Albrecht and Kübler, 2011). At least two sets of tills are present in the study area. The uppermost till dates to the retreat of the late Weichselian Fennoscandian Ice Sheet, which retreated across this part of Sweden about 11 000 years ago. Varved clays, deposited in a freshwater lake in the Baltic basin (Björck, 1995), overlie the uppermost till. Above the varved sediments, lie massive deposits of clay often grading into silt or fine-grained sand deposited during regression of Baltic waters.

The Bollnäs scarp is associated with a north–south striking nearly 12 km long topographic lineament located about 2.5 km west of the city of Bollnäs (Fig. 1). The scarp was first suggested to be ca. 8 km long (Smith et al., 2014) but with the help of large-scale airborne magnetic data and enhancement of magnetic lineaments (Fig. 2b) we found additional segments, also in the LiDAR data, in the southern parts (Fig. 2a). Our DGPS elevation measurements across the scarp show a ∼ 4–5 m difference in the topography across the scarp (Fig. 3), in agreement with the data collected by Smith et al. (2014). Based on the field observations, the scarp cross cuts surficial sediments including till, glacio-fluvial sediments, and glacial clay (Smith et al., 2014), suggesting that it is likely associated with post-glacial faulting; not from the syn-glacial periods as suggested for example for the Pärvie fault in northern Sweden (e.g., Lagerbäck and Sundh, 2008). No outcrops of basement rocks are found in the vicinity of the scarp, hence no fault or fault plane and sense of movement can directly be associated with the scarp. However, most glacially-induced faults appear to be dominantly reverse, dipping between 50 and 60° at depth (Juhlin et al., 2010; Juhlin and Lund, 2011; Ahmadi et al., 2015) and associated with zones of weakness in the bedrock (e.g., shear zones or at rock contacts). Prior to this study, existing water well data in the study area were obtained from the database of the Geological Survey of Sweden (SGU) (Fig. 3b). Well data are limited in the study area and ambiguous with one well suggesting that surficial sediments are thicker on the west side of the scarp.

SED
7, 2833–2874, 2015

In terms of seismicity, except for a recent (year 2014) magnitude 4 earthquake that occurred about 100 km west of Bollnäs, the Swedish National Seismic Network (SNSN, 2015; see also Bödvarsson and Lund, 2003) only reports very minor seismic activity in the area. Since the establishment of the modernized SNSN in the region in 2000, 36 micro-earthquakes with magnitudes in the range −0.2 to 1.4 have been recorded within 15 km of the scarp. These events do not define a linear structure, as micro-earthquakes on the post-glacial faults in northern Fennoscandia tend to (Lindblom et al., 2015), and most of the events near Bollnäs seem unrelated to the scarp.

3 Methods

Several geophysical surveys were conducted during October 2014 in one of the areas already investigated by Smith et al. (2014). Two profiles perpendicularly crossing the scarp were planned after a detailed reconnaissance prior to the surveys. While most investigations were carried out along these two profiles (Fig. 3), the focus was given to profile 1 where refraction and reflection seismic data were collected. Table 1 provides details of the acquisition parameters for the different methods. Figure 4 shows a collection of field photos from different methods used in this study. Below, we briefly describe the methods, their basis and what we measured in the study area.

3.1 Gravity and magnetic measurements

Gravity and ground magnetic measurements (Fig. 4b and d) were carried out using a LaCoste and Romberg Model G Gravity Meter and a GEM™ magnetic gradiometer. Gravity data were collected at every 10 m along profile 1 (53 points) and in scattered locations around the profile (Fig. 3) in order to provide a good indication of possible depth to bedrock in the area and to correlate with other measurements. A base station in a calm location in the study area was chosen to correct for the instrument drift and tidal variations; the base station was surveyed at least three times per day for

SED
7, 2833–2874, 2015

these purposes. All gravity points (128 data points) were surveyed accurately (less than 3 cm error for the elevation) using a DGPS geodetic surveying instrument. Figure 5a shows the free-air gravity map of the study area, which as expected follows the surface topography of the study area. Figure 5c shows the Bouguer-corrected (using a standard density of 2670 $kg\,m^{-3}$) gravity map of the study area from these measurements. A clear change in the gravity values with respect to the scarp is notable in this map. We also used other density values for the terrain correction (Fig. 5b and d) that will be discussed later.

Magnetic data, both total field and vertical gradient, were collected at 22 153 points using a walking mode (GPS-mounted) method. A base station placed away from the survey area in a calm place was used to correct for the diurnal and instrument drift. Inspection of the vertical gradient data suggested no useful information for our purposes and thus was excluded from the interpretations. However, total-field magnetic data show (Fig. 5d) a clear change in the magnetic properties on different sides of the scarp. The difference is on the order of 200 nT. Using the world magnetic model of October 2014 (http://www.ngdc.noaa.gov/geomag-web/), the earth's magnetic field intensity, inclination and declination in the study area were around 51 460 nT, 73 and 5°, respectively. No attempt was made to obtain a magnetic anomaly (through for example IGRF removal or low-order polynomial approaches) from the total-field magnetic values given the small surveyed area.

The gravity and magnetic measurements were conducted in two field campaigns (three days each) to cover a much larger area than the other data sets and after observing interesting results in the first field campaign. It was initially bound to the two profiles but expanded to cover areas in the south and north of these (Figs. 3 and 4).

3.2 Seismic survey

The refraction and reflection seismic study was carried out using a combination of a recently developed MEMs-based (micro electro-mechanical systems) 3C landstreamer (Fig. 4a; Malehmir et al., 2015a, b; Brodic et al., 2015) and 24 wireless recorders

SED
7, 2833–2874, 2015

(UNITE connected to 3C-MEMs sensors). First, wireless recorders were deployed at every 20 m along profile 1. Then a streamer (4 segments in total 200 m long and consisting of 80 3C-MEMs sensors) was used to acquire the seismic data from the southeast towards the northwest. In addition to the landstreamer and wireless recorders, 12 3C-MEMs sensors (2 m apart) were planted at the tail of the streamer to provide slightly higher fold and offset coverage. In one segment of the landstreamer, used on the tail of the profile when moving, the sensor spacing was 4 m, while in the other three segments it was 2 m. In total, the streamer had to be moved 4 times to cover profile 1 resulting in a total of 275 receiver positions. Given that the position of the wireless recorders was fixed during the survey, a maximum offset of about 480 m was achieved. A SERCEL LITE recording system was used for the data acquisition. The data sampling and time stamping was done using a built-in GPS system allowing the wireless data operating in a passive mode (continuous recording) to be harvested using the GPS times of the streamer (cabelled) data. Shooting was only carried out near the streamer sensor positions.

To generate the seismic signal, we used a 300 kg drop hammer mounted on a Bobcat (Fig. 4a; Place et al., 2015). At every shot position, three source records were generated and stacked vertically to increase the signal-to-noise ratio. In total, 256 shot positions and 29 696 seismic traces were generated. Seismic data and in particular first breaks have high quality, which allowed them to be used for refraction tomography purposes. No clear reflections could be observed in the data. Thus, neither reflection data processing nor multicompontent processing was carried out. Figure 6 shows three example shot gathers (after being vertically stacked for the repeated shot records) from the eastern, central and western sides of the scarp. A careful inspection of the direct and refracted arrivals clearly suggests a deep refractor (likely from the bedrock) on the western side of the scarp than on its eastern side. First breaks in the middle shot (Fig. 6b) suggest two possible refractors, one having lower velocity (2700 $m\,s^{-1}$) than the other (4800 $m\,s^{-1}$).

SED
7, 2833–2874, 2015

After vertically stacking of the repeated source records, the combined streamer and wireless data sets were used for first break picking. Nearly 27 800 first breaks were automatically picked (at their first energy onset), and then a careful inspection and manual correction was performed where required. Our analysis of the reciprocal times suggests an average error of nearly 2 ms for the first break picks. We used 1 ms sampling rate for the data acquisition. Figure 7a shows all travel time picks as a function of offsets.

Both refraction data analysis (e.g., generalized linear inversion 2-D ray-tracing method; Palmer, 2010) and first break tomography were performed. However, refraction data analysis was not convincing and hence is not presented.

Refraction tomography was carried out using the 3-D PStomo_eq code (Benz et al., 1996; Tryggvason et al., 2002 and Tryggvason and Bergman, 2006). The tomography code works in 3-D. Careful discretization is required in 3-D space to provide a reasonable velocity model of the subsurface. PStomo_eq uses a 2-D (or 1-D) starting model and a built-in forward solver that computes travel times for all shots and receive pairs (Hole, 1992; Podvin and Lecomte, 1991; Hole and Zelt, 1995). Backward propagation from the receiver location to the source location is then done perpendicular to the isochrones (Hole, 1992) using a ray tracing methods.

Based on a number of tests and our earlier studies using similar equipment and field set-up (Malehmir et al., 2015a, b), we chose model cell sizes of 2 m horizontal inline, 15 m horizontal crossline and 1 m vertical. This discretization was chosen so that most of the rays only cross the cells in the middle of the 3-D velocity model hence allowing the results to be presented by a 2-D vertical slice from the 3-D model.

Eight iterations were performed and an RMS misfit of 2.6 ms was obtained for the final velocity model. Figure 7b shows the travel time residuals (observed minus predicted travel times) as a function of offset for all the receiver locations. Far-offset data typically show higher misfit because of less ray coverage as opposed to the high-density ray coverage at the near surface. This means near surface materials are better resolved.

SED
7, 2833–2874, 2015

3.3 RMT and ERT surveys

The RMT method uses distant radio-transmitters (15–250 kHz) as EM sources and by measuring two components of the electric field and three components of the magnetic field it is possible to derive the resistivity structure of the subsurface (Bastani, 2001; Pedersen et al., 2006). There have been several published accounts illustrating the success of the method in resolving near surface geological structures (e.g., Bastani et al., 2009 and 2011; Shan et al., 2014). The EnviroMT equipment of Uppsala University (Fig. 4c; Bastani, 2001) was used for the RMT data acquisition. On average, 20 different frequencies could be utilized for the measurements ranging from 15 to 250 kHz. The measurements were carried out every 10 m along profiles 1 (56 stations) and 2 (49 stations). For details of RMT measurements and the underlying principals, readers are referred to Bastani (2001). Figure 8 shows three examples of apparent resistivity and phase from stations on the eastern, central and western parts of the scarp. The data quality ranges from good to very good and it is possible already from the raw data to derive a crude interpretation of the resistivity structures.

To derive resistivity models along profiles 1 and 2, we inverted the determinant response of the RMT data using EMILIA (Kalscheuer et al., 2008), which is a modified version of the REBOCC program (Siripunvaraporn and Egbert, 2000). Inversion of determinant data is recommended because the determinant data are rotationally invariant but also smoothens out 3-D effects in the 2-D inversion (Pedersen and Engels, 2005). The program is based on a finite difference technique and hence optimal mesh design is an important factor to be considered. To set up the model, we used 1 m cells at the top of the model that increase vertically with a geometrical progression of 1.12 down to 1200 m depth (only the first 100 m are of interest in our case). The horizontal cells were fixed as two blocks per measuring point i.e. 5 m. A starting model of homogeneous half space with 1000 Ω m and Occam-type regularization was used. With an error floor of 4 % on apparent resistivity and phase, resistivity models with an average RMS error of about 2.8 were obtained for both profiles.

SED
7, 2833–2874, 2015

ERT is a fast and relatively inexpensive geophysical method commonly used for near surface applications (Stummer et al., 2004; Günther and Rücker, 2006a, b; Paasche, 2006; Loke, 2014; Reynold, 2011; Shan et al., 2014). The method is based on detecting differences in resistivity of the subsurface materials. In contrast to the RMT method, which is primarily sensitive to conductive structures, ERT is more sensitive to resistive targets. Typically, a four-electrode array (electrode spread) is employed, where two electrodes are used to induce the electrical current into the ground (current electrodes), while the remaining two are used to measure the resulting potential difference (Loke, 2010). Depending on the number of electrodes used and their position along the surface, numerous configurations (arrays) exist to optimize the data acquisition. The arrays may be spatial (like dipol-dipol or square arrays) or collinear (Wenner, Schlumberger, Pole-pole, Gradient array, etc.). The selection of the array directly determines whether the measurements will result in a 1-D resistivity profile, a 2-D resistivity section or a 3-D resistivity volume.

In our study, we used the ABEM Terameter™ LS. Both profiles were acquired using the Gradient array (Dahlin and Zhou, 2006) and an electrode spacing of 5 m. The advantage of this array type over the other arrays is higher penetration depth and lower degree of data loss at the edges of the survey lines (Dahlin and Zhou, 2006). Profile 1 was 400 m long while profile 2 was 700 m long and required a roll-along (Günther, 2004) acquisition. We used 300 m overlap between the two consecutive segments implying an increment of 100 m for the measurements.

Data inversion was carried out using DC2DInvRes (Günther, 2004; Günther and Rücker, 2006a, b). The inversion was done incorporating topography for both lines with horizontal grid spacing of 5 m and vertical grid spacing of 2.5 m. The final models used for the interpretation had RMS errors of 4.8 and 4.2 for profiles 1 and 2, respectively.

3.4 GPR and geodetic surveys

Electro-magnetic waves used in the GPR method can be reflected by geological interfaces such as sediment/crystalline basement interface or syn-sediment features (e.g.,

SED
7, 2833–2874, 2015

Dehls et al., 2000; Reynolds, 2011), provided that these interfaces coincide with discontinuities in the electrical and dielectric properties. GPR investigations were therefore justified in the Bollnäs case to tentatively help delineate the top of the basement or the inner structure of the sediments. Two 100 MHz antennas one acting as transmitter and another as receiver were used for the data acquisition. Uniform sampling along the profile was ensured by using a thread pulled along with the acquisition system as a trigger. Several GPR profiles were measured, either at high angle or sub-parallel to the scarp (Fig. 3).

Geodetic positioning of all the stations for all the different surveys was carried out using a DGPS system (Fig. 4b) with precision of a few centimetres both horizontally and vertically. The GPS signal was excellent due to the open space with no dense tree coverage. Magnetometry data collected in the forest areas still showed a good quality GPS signal.

4 Results and interpretations

Before we present the results, in the following we define the bedrock depth as the vertical distance between the top of the bedrock and the surface (given in negative values) and the bedrock level as compared to the real topography i.e., sea level (given in positive values).

Total field magnetic data depict a magnetic lineament about 50–60 m west of the scarp (Fig. 9) suggesting a sharp change in the bedrock depth or nature at this location. This is consistent with the large-scale airborne magnetic data from the study area (Fig. 2b). Tests with reduction to the magnetic pole did not significantly move the location of the magnetic lineament because of the high geographic latitude of the study area (earth's magnetic field is nearly vertical). The magnitude of the total magnetic field, while showing local variations, is in general higher on the eastern side of the scarp than on the western side by nearly 200 nT. If we assume the magnetic response to be solely due to a crystalline bedrock that is magnetically uniform in our study area,

SED
7, 2833–2874, 2015

this result suggests that the bedrock, contrary to our expectation, is at shallower depths on the eastern side of the scarp than on the western side. Alternatively one can argue that there are more glacial and post-glacial sediments on the western side of the scarp forming the apparent topography in the study area. Assuming that the magnetic lineament is caused by a vertical fault displacing the bedrock, the fault would then be located in the inflection point in the transition from magnetic high to low (Hinze et al., 2013), somewhere roughly between the LiDAR lineament and the magnetic lineament (Fig. 9b; see also the dashed line in Fig. 9). A dipping fault would slightly shift the location to the down-dip (i.e., slightly towards the magnetic lineament). Using the rule-of-thumb half-width criteria (Hinze et al., 2013), depth of the underlying magnetic body (assumed to be the bedrock) would be at about −25 m on the western side of the scarp.

Using a standard density of 2670 kg m^{-3} to obtain Bouguer anomaly data (topographic correction) in the study area results on gravity higher (nearly 0.5 mgal) on the eastern side of the scarp than on its western side (Figs. 5c and 10b). We decided to use smaller values to represent density of the sediments forming the topography. We tested various densities possible for glacial and post-glacial sediments (Salas-Romero et al., 2015) such as 1800 and 2200 kg m^{-3} as shown in Figs. 5b and 10b. Interestingly, densities around 2200 kg m^{-3} result in a Bouguer anomaly that is nearly uniform (or only 0.1 mgal higher) on both sides of the scarp (Fig. 10b) particularly along the two profiles (Fig. 5b). This may suggest that there is no detectable bedrock level difference from one side of the scarp to another. Using the half-width rule and the standard Bouguer gravity data, the fault location and depth to the body would be similar to that of the magnetic data (i.e., ∼ −25 m). No matter which density is used for the Bouguer correction, there seems to be denser materials on the western side of the scarp than on the eastern side (Fig. 5b and c). In fact, there is a good similarity between the Bouguer map when 2670 kg m^{-3} is used for elevation correction and the total field magnetic map (Fig. 5c and d).

RMT results along both profiles (Figs. 10 and 11) consistently show a major high conductivity zone apparently dipping to the west slightly west of the scarp. Given that

SED
7, 2833–2874, 2015

RMT data are sensitive to conductive materials and the top of the conductive materials are often better resolved, we believe the conductive anomaly is real and may represent a major water-bearing zone, whose porosity could be related to a brittle deformation zone in the bedrock. The top of the bedrock is also somewhat resolved but not as well as the conductor. It is not possible to clearly estimate any throw and displacement in the bedrock from the RMT data either. Nevertheless, it is possible to infer thicker sediment cover on the western side of the scarp than on the eastern side particularly along profile 2 (Fig. 11b).

ERT data are much more sensitive to resistive materials and thus should be able to resolve better the top of the bedrock. Unfortunately the ERT line along profile 1 is shorter than the other line (profile 2). Nevertheless, the bedrock surface and a major conductivity zone west of the scarp are also consistently evident in the ERT results (Fig. 12). Similar to the RMT results, ERT results also suggest the bedrock surface at more or less the same level. Hence it is difficult to estimate fault throw from these data as well. It is likely not higher than five meters based on the data from the southeastern side of profile 2 (Fig. 12b).

Tomography results (Fig. 10d) suggest similar structures as ERT and RMT data along profile 1; a major low-velocity zone at the scarp location and slightly towards the west of it. Bedrock represented by high velocity materials is clearly deeper on the western side of the scarp than on the eastern side. However, a careful inspection of the results suggests that the covered sediments are likely much thicker on the western side (about −20 m) of the scarp implying a bedrock level more or less at the same level in both sides of the scarp. A major low-velocity zone at about 300–400 m distance along profile 1, where the scarp and magnetic lineaments are located (Fig. 10d), is likely the result of a zone of highly fractured rocks or a depression in the bedrock that is filled with glacial and post-glacial sediments. This is consistent with the depth estimates from the gravity and magnetic data at the interpreted fault location. Similar as with all the other data, it is difficult to infer any potential cumulated fault throw from the seismic data. This will be discussed later.

SED
7, 2833–2874, 2015

In most of the GPR profiles, a shallowly (2–5°) easterly dipping reflection between −2 to −5 m depth was observed immediately east of the scarp (Fig. 13a). The GPR depth penetration is quite restricted in the area, presumably as a consequence of the high clay content of the sediments. We believe GPR data do not provide any information from the bedrock and the reflection observed likely occurs within the glacial sediments overlying the crystalline basement. During the trenching at the site, Smith et al. (2014) noted a gently dipping (3–5°) till underlying silt and varved clays at depths around −3 m (Fig. 13b and c). The reflection in the GPR data is likely generated at the contact between till and these materials. It is a common feature when the scarp is crossed up to about 300 m distance in the northern side of profile 1. We observed this in more than 5 short GPR transects (blue points north of profile 2 in Fig. 3). It is remarkable that we observe only one reflection in the GPR data and only on the eastern side of the scarp. It is possible that the lack of continuity in the western-end of side of the GPR reflection at roughly where the scarp starts is an indication for faulted sediments. The reflection may also be from groundwater table and its interruption in the western side (Fig. 13c) due to water flowing suddenly into the faulted bedrock. Smith et al. (2014) reported a pronounced depression in the water-table surface along the scarp at one of the trenches the made in northern parts of the study area.

5 Discussion

The multiple geophysical methods used to study the Bollnäs scarp suggest a major structure in the bedrock about 20–30 m west of the LiDAR lineament. In order to illustrate the consistency among the different results, a 3-D visualization of all the results with surface geology and LiDAR data is shown in Fig. 14. Here, we discuss scenarios that can plausibly explain the scarp in light of the results and existing knowledge from available post-glacial faults. It is important to note that in the absence of direct observations (i.e., boreholes) most of the discussion and interpretation of the geophysical data is speculative and may change as new data arrive from the site.

SED
7, 2833–2874, 2015

5.1 Origin of the Bollnäs scarp and role of earlier structures

One of the objectives of the study was to relate the Bollnäs scarp to features in the bedrock. We suggest that there is a relationship between the scarp and the high-conductivity and low-velocity structures observed in the bedrock from ERT, RMT and seismic data. There is a major brittle structure in the bedrock causing the low-velocity and high-conductivity zone observed in these data. This can be linked to post-glacial fault movement forming the LiDAR lineament but also points towards pre-existing structures. Magnetic lineaments, seismically anomalous and conductive zones have also been reported to be associated with topographic lineaments elsewhere in central Sweden (e.g., Malehmir et al., 2011), nevertheless interpreted to be associated with multi-phase deformation zones and not to any post-glacial faulting. It is difficult to explain why the bedrock is shallower on the eastern side of the scarp than on the western side if we expect the fault to be post-glacial and have recent reverse kinematics. It is unlikely that the Bollnäs scarp formed as a result of normal faulting (e.g., Dehls et al., 2000) because of the apparent surface morphology suggesting an upthrow on the western side and shallower bedrock on the eastern side.

To explain all the results, we relate the Bollnäs scarp to an earlier structure in the bedrock, likely a multi-phase deformation zone (Fig. 2) that acted as a normal fault much earlier (e.g., > 1.8 Ga). This means that the bedrock level was already at deeper levels on the western side of the scarp sometimes prior to the Weichselian deglaciation (~ 11 000 years ago). The erosion of older sediments and deposition of Weichselian glacial and post-glacial sediments resulted in thicker sediments on the western side of the scarp (Fig. 15). During deglaciation, the deformation zone was reactivated as a reverse fault triggered by the combination of tectonic and glacially induced stresses (Lund et al., 2015). Quaternary geologic data suggests a single rupture at about 10 200 BP (Smith et al., 2014).

The large-scale magnetic data (Fig. 2b) suggest that there are numerous magnetic lineaments in the study area one of which is clearly associated with the Bollnäs scarp.

SED
7, 2833–2874, 2015

We think these magnetic lineaments (N–S and E–W trending) are evidence for pre-existing structures. Magnetic minima then would result from fluid circulation and alteration of magnetic minerals in these zones. Isaksson (2008) reported magnetic minima from deformation zones in central Sweden as a result of hematization of magnetic because of hydrothermal alteration.

The geophysical results suggest a moderately ($\sim 45^{\circ}$) westward dip for the deformation zone (Fig. 14). Interestingly most post-glacial faults in northern Sweden show a throw opposite to what we infer for the Bollnäs fault. They are often down on the western side of the fault as opposed to the eastern side here. Again, this is likely controlled by pre-existing structures and illustrates their role in controlling the geometry and location of post-glacial faults in Sweden.

5.2 Possible earthquake magnitude

Assuming that the Bollnäs scarp is due to a post-glacial fault taking advantage of a pre-existing structure in the bedrock, we can only speculate on the magnitude of the associated earthquake(s) from some of the available data. We first assume that the Bollnäs scarp was formed as one event (Smith et al., 2014). Although we do not have evidence for it at this stage the assumption is conservative from a safety assessment perspective (see also McCalpin, 1996). According to Stewart and Hancock (1990), a single piedmont scarp is likely the product of a single increment of motion when the scarp displays characteristic morphology comprising of a steep ($> 50^{\circ}$) free surface, a moderately inclined (30–40°) debris slope and a gently inclined (5–10°) washed slope. Some of these characteristics are consistent with the Bollnäs scarp (Fig. 10a) and may support our assumption.

Leonard (2010) points out that for dip-slip events in stable continental regions, assuming that the surface rupture length is equal to the subsurface rupture length fits the data better than previously proposed relations between the two. We will therefore assume here that the total length of the scarp, 12 km, equals the rupture length in the event. We further consider the 5 m high scarp as a proxy for the bedrock displacement

SED
7, 2833–2874, 2015

that took place during the suspected earthquake. This is, however, a poorly constrained relation, which we discuss further below. Using the empirical equations of Leonard (2010) we estimate the possible magnitude of the Bollnäs event in two different ways. First using only the rupture length (L) as input data and the equation (Leonard, 2010):

$$\log(M_0) = 2.5\log(L) + 8.08, \quad (1)$$

with the usual relation between M_0 (scalar seismic moment) and M_w (moment magnitude):

$$M_w = 2\log(M_0)/3 - 6.07, \quad (2)$$

resulting in a magnitude $M_w = 6.1$.

Secondly, we estimate the magnitude from the width (W) of the fault plane using (Leonard, 2010):

$$W = 13.5(L^{2/3}). \quad (3)$$

With that and the assumption that the height of the scarp equals the maximum slip in the event and that the average displacement (D) is approximately half of the maximum displacement (Leonard, 2010), we can calculate:

$$M_0 = \mu W L D, \quad (4)$$

which results in a magnitude $M_w = 6.5$ (using Eq. 2) for $\mu = 33$ GPa (shear modulus; Leonard, 2010). We note that the Leonard (2010) regressions for average displacement in a 12 km rupture length earthquake is only 0.67 m. This could indicate that we significantly overestimate the average slip using the scarp height or underestimate the length of the fault. It is however in agreement with the observation by Muir-Wood (1989) that post-glacial earthquakes in northern Fennoscandia are short relative to their vertical offsets. With the data we have, we consider it likely that the Bollnäs scarp was created in a single large rupture; the associated magnitude would have probably been approximately 6–6.5.

SED
7, 2833–2874, 2015

5.3 Future studies

To prove that there is actually a post-glacial fault in the bedrock causing the Bollnäs scarp, a shallow drilling program is suggested. A couple of 50–100 m deep inclined holes (Fig. 14a) would be required to pass through the crushed rocks until fresh bedrock east of the scarp is observed. Locating the actual post-glacial fault plane may be difficult to impossible if only visual inspection of the core samples is used because of its interpreted multi-stage deformation nature. Therefore, a careful sampling and analysis of clay mineralogy and possibly age would be required to pin-point that the crushed zone in fact hosts a post-glacial fault. More attention can also be given to the glacial sediments above the bedrock and if possible undisturbed samples from these sediments to be taken for detailed studies of changes in the stratigraphy due to the post-glacial faulting. Downhole geophysical logging and possibly imagery and hydraulic testing should follow the drilling. It is possible that rocks at the fault zone are so fractured and mixed with the sediments that these together make the apparent thicker sediments on the western side of the scarp than its eastern side. Thus, the drilling plan should be carefully considered and perhaps first be done (prior to coring) at regular points to define the bedrock level across the scarp. Other places where possibly bedrock is shallower should be considered for further trenching.

To observe the depth extent of the fault, a longer seismic profile similar to that carried out by Juhlin et al. (2010) also in conjunction with the magnetotellurics methods is recommended. Recently hydro-acoustical and marine seismic data aiming at tracing the Bollnäs scarp across the lake Voxsjön were acquired. Results are not available yet. We further suggest geophysical studies such as boat-towed RMT (Bastani et al., 2015) to provide information about the depth to the bedrock on both sides of the scarp in the lake. Given the fresh nature of the water in the lake, RMT data acquisition is possible. Joint inversion of multiple datasets (e.g., Bastani et al., 2012) can also be performed although we do not believe these can resolve the bedrock offset since bedrock is likely highly fractured and has no sharp surface to be resolved.

SED
7, 2833–2874, 2015

6 Conclusions

Several different surface geophysical methods were utilized to better understand the relationship between the Bollnäs scarp and potential structures in the bedrock. The multiple methods provided consistent results allowing for a reliable interpretation to be given. The Bollnäs scarp was found to be associated with a magnetic lineament, a major low-velocity and high-conductivity zone in the bedrock. Despite a noticeable 4–5 m topographic high on the western side of the scarp, the geophysical results suggested more or less similar bedrock levels on both sides, the only difference being thicker sediment cover on the western side than the eastern side. The thicker sediment on the western side explains the gravity low and magnetic low on the same side supporting our interpretation of the data. The Bollnäs scarp is likely associated with a pre-existing structure, a multi-phase deformation zone, in the bedrock that was interpreted to have at some stages acted as a normal fault allowing thicker deposition of glacial and post-glacial sediments prior to the post-glacial faulting forming the LiDAR lineament in the study area. The location and geometry of the Bollnäs fault is interpreted to be solely controlled by this deformation zone. Based on the new finding for the length of the scarp and a series of assumptions, we estimate that the Bollnäs scarp was generated by a magnitude 6–6.5 earthquake and likely as a single event. Further studies, particularly drilling and large-scale geophysical studies, would be required to confirm and evaluate the interpretation of the geophysical data provided in this study.

Acknowledgements. Swedish nuclear waste management company (SKB), Formas (http://trust-geoinfra.se), Geophysics Program of Uppsala University and Geological Survey of Sweden provided partial funding and support to carry this study. Several MSc and PhD students as well as field teachers took part in the data acquisition and preparation of the data during the applied and exploration geophysics course (October 2014) for which we are grateful. GLOBE Claritas™ under license from the Institute of Geological and Nuclear Sciences Limited, Lower Hutt, New Zealand was used to process the seismic data. Refraction tomography was carried out using the 3-D PStomo_eq code (provided by Ari Tryggvason), RMT inversion using EMILIA (provided by Thomas Kalscheuer) and ERT inversion using DC2DInvRes (provided by Thomas

SED
7, 2833–2874, 2015

Günther). gOcad™ consortium and Paradigm are thanked for providing an academic license of gOcad™ for 3-D visualization and interpretation of the data. GMT from P. Wessel and W.H.F. Smith, Matlab and gOcad™ were used to prepare some of the figures.

References

Ahmadi, O., Juhlin, C., Ask, M., and Lund, B.: Revealing the deeper structure of the end-glacial Pärvie fault system in northern Sweden by seismic reflection profiling, Solid Earth, 6, 621–632, doi:10.5194/se-6-621-2015, 2015.

Albrecht, L. and Kübler, L.: Bedrock Map 15G Bollnäs, scale 1 : 250 000, Geological Survey of Sweden, Uppsala, Sweden, K312, 2011.

Arvidsson, R.: Fennoscandian earthquakes: whole crustal rupturing related to postglacial rebound, Science, 274, 744–746, 1996.

Bastani, M.: EnviroMT- A New Controlled Source/Radio Magnetotelluric System, Ph.D thesis, Acta Universitatis Upsaliensis, Uppsala Dissertations from the Faculty of Science and Technology, Uppsala, 32, 2001.

Bastani, M., Malehmir, A., Ismail, N., Pedersen, L. B., and Hedjazi, F.: Delineating hydrothermal stockwork copper deposits using controlled-source and radio-magnetotelluric methods: a case study from northeast Iran, Geophysics, 74, B167–B181, 2009.

Bastani, M., Savvaidis, A, Pedersen, L. B., and Kalscheuer, T.: CSRMT measurements in the frequency range of 1–250 kHz to map a normal fault in the Volvi basin, Greece, J. Appl. Geophys., 75, 180–195, doi:10.1016/j.jappgeo.2011.07.001, 2011.

Bastani, M., Hübert J., Kalscheuer, T., Pedersen, L. B., Godio, A., and Bernard, J.: 2-D joint inversion of RMT and ERT data versus individual 3-D inversion of full tensor RMT data: an example from Trecate site in Italy, Geophysics, 77, WB233–WB243, doi:10.1190/GEO2011-0525.1, 2012.

Bastani, M., Persson, L., Mehta, S., and Malehmir, A.: Boat-towed radio-magnetotellurics (RMT) – a new technique and case study from the city of Stockholm, Geophysics, doi:10.1190/GEO2014-0527.1, online first, 2015.

Benz, H. M., Chouet, B. A., Dawson, P. B., Lahr, J. C., Page, R. A., and Hole, J. A.: Three dimensional P- and S-wave velocity structure of Re- doubt volcano, Alaska, J. Geophys. Res., 101, 8111–8128, 1996.

SED
7, 2833–2874, 2015

Brandes, C., Winsemann, J., Roskosch, J., Meinsen, J., Tanner, D. C., Frechen, M., Steffen, H., and Wu, P.: Activity of the Osning thrust during the late Weichselian: ice-sheet and lithosphere interactions, Quaternary Sci. Rev., 38, 49–62, doi:10.1016/j.quascirev.2012.01.021, 2012.

Brandes, C., Steffen, H., Steffen, R., and Wu, P.: Intraplate seismicity in northern Central Europe is induced by the last glaciation, Geology, 43, 611–614, 2015.

Brodic, B., Malehmir, A., Juhlin, C., Dynesius, L., Bastani, M., and Palm, H.: Multicomponent broadband digital-based seismic landstreamer for near surface applications, J. Appl Geophys., in revision, 2015.

Björck, S.: A review of the history of the Baltic Sea, 13.0–8.0 ka BP, Quaternary Int., 27, 19–40, 1995.

Bödvarsson, R. and Lund, B.: The SIL seismological data acquisition system -as operated in Iceland and in Sweden, in: Methods and applications of signal processing in seismic network operations, edited by: Takanami, T. and Kitagawa, G., Lecture Notes in Earth Sciences 98, Springer, Berlin, Germany, 131–148, 2003.

Dahlin, T. and Zhou, B. Multiple-gradient array measurements for multichannel 2-D resistivity imaging, Near Surface Geophysics, 4, 113–123, 2006.

Dehls, J. F., Olesen, O., Olsen, L., and Blikra, L.H: Neotectonic faulting in northern Norway; the Stuoragurra and Nordmannvikdalen post-glacial faults, Quarternary Sci. Rev., 19, 1447–1460, 2000.

Günther, T.: Inversion methods and Resolution Analysis for the 2-D/3-D Reconstruction of Resistivity Structures from DC measurements, PhD Thesis, University of Mining and Technology, Freiberg, 2004.

Günther, T.: Roll-Along-Inversion – A New Approach For Very Long DC Resistivity Profiles, EAGE Near Surface Geophysics, Istanbul, 2006.

Günther, T. and Rücker, C.: A General Approach for Introducing Information Into Inversion and Examples From DC Resistivity Inversion, EAGE Near Surface Geophysics, Helsinki, Finland, 2006a.

Günther, T. and Rücker, C.: A New Joint Inversion Approach Applied to the Combined Tomography of DC Resistivity and Seismic Refraction Data, 19th Symposium on the Application of Geophysics to Engineering and Environmental Problems (SAGEEP 2006), Seattle, USA, 2–6 April, 2006b.

SED
7, 2833–2874, 2015

Isaksson, H.: Magnetic lineaments and their relationship to ductile structures and steeply dipping fracture zones at Forsmark, Fennoscandian Shield, Sweden, International Geological Congress, Oslo, available at: http://www.cprm.gov.br/33IGC/1316395.html (last access: 7 October 2015), 2008.

Jakobsson, M., Björck, S., O'Regan, M., Flodén, T., Greenwood, S. L., Swärd, H., Lif, A., Ampel, L., Koyi, H., Skelton, A.: Major earthquake at the Pleistocene-Holocene transition in Lake Vättern, southern Sweden, Geology, 42, 379–382, 2014.

Juhlin, C. and Lund, B.: Reflection seismic studies over the end-glacial Burträsk fault, Skellefteå, Sweden, Solid Earth, 2, 9–16, doi:10.5194/se-2-9-2011, 2011.

Juhlin, C., Dehghannejad, M., Lund, B., Malehmir, A., and Pratt, G.: Reflection seismic imaging of the end-glacial Pärvie fault system, northern Sweden, J. Appl. Geophys., 70, 307–316, 2010.

Hinze, W. J., Von Frese, R. R. B., and Saad, A. H.: Gravity and Magnetic Exploration, Cambridge University Press, Cambridge, UK, 2013.

Hole, J. A.: Nonlinear high-resolution three-dimensional seismic traveltime tomography, J. Geophys. Res., 97, 6553–6562, 1992.

Hole, J. A. and Zelt, B. C.: 3-D finite-difference reflection traveltimes, Geophys. J. Int., 121, 427–434, 1995.

Kalscheuer, T., Pedersen, L. B., and Siripunvaraporn, W.: Radiomagnetotelluric two-dimensional forward and inverse modelling accounting for displacement currents, Geophys. J. Int., 175, 486–514, 2008.

Kuivamäki, A., Vuorela, P., and Paananen, K.: Indications of postglacial and recent bedrock movements in Finland and Russian Karelia, Geolological Survey of Finland, Helsinki, Finland, Report YST-99, 1998.

Lagerbäck, R. and Sundh, M.: Early Holocene faulting and paleoseismicity in northern Sweden, Tech. Rep. C 836, Geological Survey of Sweden, Uppsala, Sweden, 2008.

Leonard, M.: Earthquake fault scaling: self-consistent relating of rupture length, width, average displacement, and moment release, B. Seismol. Soc. Am., 100, 1971–1988, 2010.

Lindblom, E., Lund, B., Tryggvason, A., Uski, M., Bödvarsson, R., Juhlin, C., and Roberts, R.: Micro-earthquakes illuminate the deep structure of the end-glacial Pärvie fault, northern Sweden, Geophys. J. Int., 201, 1704–1716, 2015.

SED
7, 2833–2874, 2015

Loke, M. H.: Electrical resistivity surveys and data interpretation, in: Solid Earth Geophysics Encyclopedia, 2nd Edn. “Electrical and Electromagnetic”, edited by: Gupta, H., Springer-Verlag, the Netherlands, 276–283, 2014.
Lund, B.: Palaeoseismology of glaciated terrain, Springer Encyclopedia of Earthquake Engineering, Springer, Berlin, doi:10.1007/978-3-642-36197-5_25-1, 2015.
Lund, B., Schmidt, P., and Hieronymous, C.: Stress evolution and fault stability during the Weichselian glacial cycle, Tech. Rep. TR-09-15, Swedish Nuclear Fuel and Waste Manage. Co. (SKB), Stockholm, Sweden, available at: www.skb.se/publications, last access: 26 March 2015.
Malehmir, A., Dahlin, P., Lundberg, E., Juhlin, C., Sjöström, H., and Högdahl, K.: Reflection seismic investigations in the Dannemora area, central Sweden: insights into the geometry of poly-phase deformation zones and magnetite-skarn deposits, J. Geophys. Res., 116, B11307, doi:10.1029/2011JB008643, 2011.
Malehmir, A., Wang, S., Lamminen, J., Brodic, B., Bastani, M., Vaittinen, K., Juhlin, C., and Place, J.: Delineating structures controlling sandstone-hosted base-metal deposits using high-resolution multicomponent seismic and radio-magnetotelluric methods: a case study from Northern Sweden, Geophys. Prospect., 63, 774–797, doi:10.1111/1365-2478.12238, 2015a.
Malehmir, A., Zhang, F., Dehgahnnejad, M., Lundberg, E., Döse, C., Friberg, O., Brodic, B., Place, J., Svensson, M., and Möller, H.: Planning of urban underground infrastructure using a broadband seismic landstreamer – Tomography results and uncertainty quantifications from a case study in southwest of Sweden, Geophysics, 80, B177–B192, 2015b.
McCalpin, J. P.: Paleoseismology, Academic Press, New York, USA, 1996.
Mikko, H., Smith, C.A, Lund, B., Ask, M., and Munier, R.: LiDAR-derived inventory of post-glacial fault scarps in Sweden, Journal of the Geological Society of Sweden, doi:10.1080/11035897.2015.1036360, online first, 2015.
MuirWood, R.: Extraordinary deglaciation reverse faulting in northern Fennoscandia, in: Earthquakes at North-Atlantic Passive Margins: Neotectonics and Postglacial Rebound, edited by: Gregersen, S. and Basham, P. W., NATO ASI Series, Denmark, 141–173, 1989.
Mörner, N.-A.: Active faults and paleoseismicity in Fennoscandia, especially Sweden, primary structures and secondary effects, Tectonophysics, 380, 139–157, 2004.
Mörner, N.-A.: Paleoseismology: the application of multiple parameters in four case studies in Sweden, Quatern. Int., 242, 65–75, doi:10.1016/j.quaint.2011.03.054, 2011.

SED
7, 2833–2874, 2015

Olesen, O., Kierulf, H. P., Brönner, M., Dalsegg, E., Fredin, O., and Solbakk, T.: Deep weathering, neotectonics and strandflat formation in Nordland, northern Norway, Norwegian J. Geol., 93, 189–213, 2013.

Olesen, O., Blikra, L. H., Braathen, A., Dehls, J. F., Olsen, L., Rise, L., Riis, F., Faleide, J. I., and Anda, E.: Neotectonic deformation in Norway and its implications: a review, Norwegian J. Geol., 84, 3–34, 2004.

Palmer, D.: Characterizing the near surface with detailed refraction attributes, in: Advances in Near-Surface Seismology and Ground-Penetrating Radar, edited by: Miller, R. D., Bradford, J. H., and Holliger, K., Geophysical Developments Series, SEG, Tusla, USA, 15, 233–249, 2010.

Paasche, H. Characterization of alluvial aquifers using geophysical techniques: integrated surveying strategies and case studies, Federal Institute of Technology, Zurich, 2006.

Pedersen, L. B. and Engels, M.: Routine 2-D inversion of Magnetotelluric data using the determinant of the impedance tensor, Geophysics, 70, G33–G41, 2005.

Pedersen, L. B., Bastani, M., and Dynesius, L.: Some characteristics of the electromagnetic field from radio transmitters in Europe, Geophysics, 71, G279–G284, doi:10.1190/1.2349222, 2006.

Place, J. A. P., Malehmir, A., Högdahl, K., Juhlin, C., and Persson Nilsson, K.: Seismic characterization of the Grängesberg iron deposit and its mining-induced structures, central Sweden, Interpretation, 3, SY41–SY56, 2015.

Podvin, P. and Lecomte, I.: Finite difference computation of traveltimes in very contrasted velocity models: a massively parallel approach and its associated tools, Geophys. J. Int., 105, 271–284, 1991.

Reynolds, J. M.: An Introduction to Applied and Environmental Geophysics, 2nd Edn., Wiley, Chichester, UK, ISBN: 978-0-471-48535-3, 2011.

Salas-Romero, S., Malehmir, A., Snowball, I., Lougheed, B. C., Hellqvist, M.: Identifying landslide preconditions in Swedish quick clays – insights from integration of surface geophysical, core sample- and downhole-property measurements, Landslides, doi:10.1007/s10346-015-0633-y, online first, 2015.

Siripunvaraporn, W. and Egbert, G.: An efficient data-subspace inversion method for two-dimensional magnetotelluric data, Geophysics, 65, 791–803, 2000.

SED
7, 2833–2874, 2015

Shan, C., Bastani, M., Malehmir, A., Persson, L., and Engdahl, M.: Integrated 2-D modelling and interpretation of geophysical and geotechnical data to delineate quick clays at a landslide site in southwest Sweden, Geophysics, 79, EN61–EN75, doi:10.1190/GEO2013-0201.1, 2014.
Smith, C., Sundh, M., and Mikko, H.: Surficial geologic evidence for early Holocene faulting and seismicity, Int. J. Earth Sci., 103, 1711–1724, 2014.
Stewart, I. S. and Hancock, P. L.: Brecciation and fracturing within neotectonic normal fault zones in the Aegean region, in: Deformation Mechanisms, Rheology and Tectonics, edited by: Knipe, R. J. and Rutter, E. H., Geol. Soc. Spec. Publ., 54, 105–112, 1990.
Stummer, P.; Maurer, H., and Green, A. G. Experimental design: electrical resistivity data sets that provide optimum subsurface informationm, Geophysics, 69, 120–139, 2004.
SNSN: Earthquake locations, Swedish National Seismic Network, Uppsala University, Sweden, l, available at: www.snsn.se, last access: August, 2015.
Sukotjo, S. and Sträng T.: Bedrock Map 14G Ockelbo NO, scale 1 : 50 000, Geological Survey of Sweden, Helsinki, Finland, K22, 2005.
Tryggvason, A. and Bergman, B.: A travel time reciprocity inaccuracy in the time 3d finite difference algorithm by Podvin and Lecomte, Geophys. J. Int., 165, 432–435, 2006.
Tryggvason, A., Rögnvaldsson, S. T., and Flovenz, Ó. G.: Three dimensional imaging of P- and S-wave velocity structure and earthquake locations beneath southwest Iceland, Geophys. J. Int., 151, 848–866, 2002.
Wu, P., Johnston, P., and Lambeck, K.: Postglacial rebound and fault instability in Fennoscandia, Geophys. J. Int., 139, 657–670, 1999.

SED
7, 2833–2874, 2015

Table 1. Summary of some the acquisition parameters, October 2014.

Survey type	Seismic	ERT	RMT	Gravity and magnetic
Acquisition system	SERCEL Lite 428	ABEM™	EnviroMT	Lacoste and Romberg and GEM™
No. of receivers	80-3C landstreamer, 12-3C plant and 24-3C wireless	48	5 (2 E-field and 3 Mag-field)	128 gravity points and 22 153 magnetic points
No. of source points	256	–	Up to 20 transmitters	–
Receiver interval	2–4 m (streamer) and 20 m wireless recorders	2–4 m	10 m	10 m (gravity) and 1–2 m (magnetic)
Shot interval	10 m	4 m	–	–
Source-receiver offset	480 m	160 m	–	–
Source size	Bobcat 300 kg drop hammer	–	Passive (14–250 kHz)	–
Profile length	600 m (P1)	400 m (P1) and 720 m (P2)	560 m (P1) and 490 m (P2)	600 m (P1) and 500 m (P2) also at scattered locations
Spread				
Record length	10 s (1 s used)	–	50 times power stacking	–
Sampling rate	1 ms	–	2 MHz	Walking mode (magnetic)
Sensor	3C-MEMs	48	Electric and magnetic fields	Vertical (gravity) and Total-field (magnetic)
No. of sensors	Single	Multiple	Two horizontal E-field and two horizontal and one vertical magnetic	–
Pattern	3 impacts/point	Gradient array	Vertical electrical dipoles	–

SED
7, 2833–2874, 2015

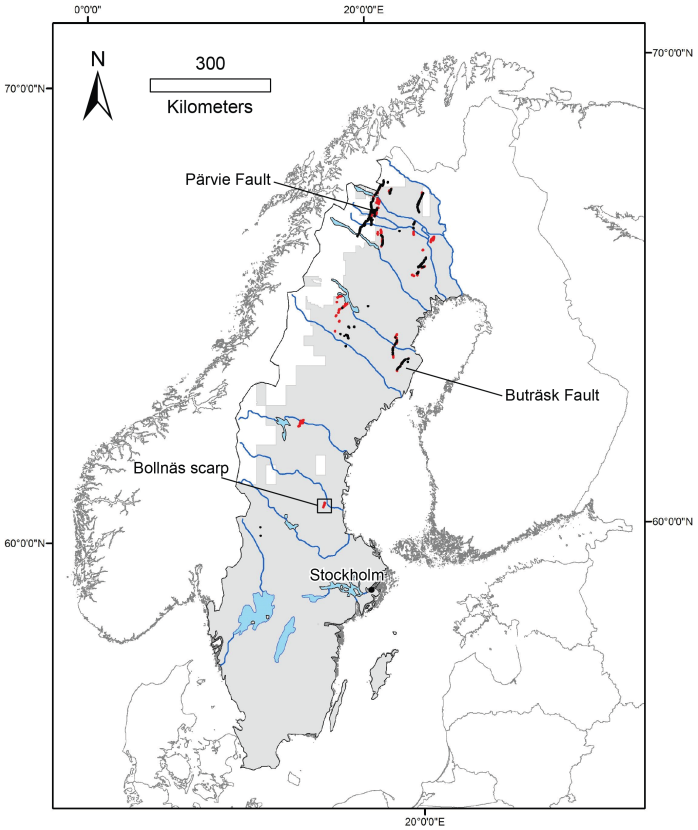

Figure 1. Inferred location of the post-glacial faults in Sweden. Bollnäs prospective fault being much smaller in size and length was recently discovered from LiDAR-imagery (shaded regions) as a 4–5 m high scarp is the focus of this study. Red-dots show the locations of LiDAR scarps and black dots known post-glacial faults (e.g., Pärvie and Burträsk).

SED
7, 2833–2874, 2015




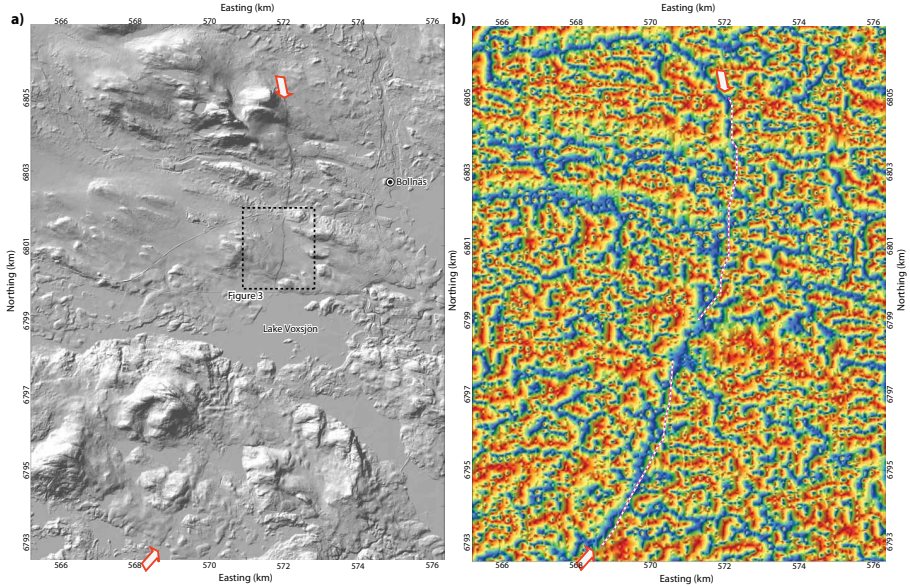

Figure 2. (a) Shaded relif LiDAR map and **(b)** tilt-derivative of total-field aeromagnetic map showing the Bollnäs scarp and noticeable magnetic lineament (blue magnetic low, red magnetic high) associated with it. The scarp occurs slightly east of the magnetic lineament following it for about 12 km distance. LiDAR data were provided by Lantmäteriet and magnetic data by the Geological Survey of Sweden.

SED
7, 2833–2874, 2015

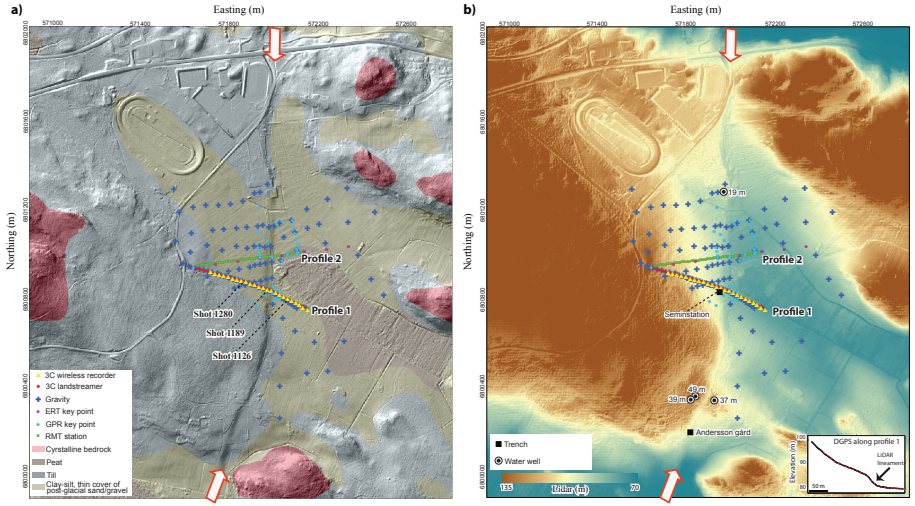

Figure 3. (a) Surface geological map (Courtesy of the Geological Survey of Sweden) of the Bollnäs area projected onto hill-shaded LiDAR topographic data (Courtesy of Lantmäteriet) showing a clear scarp that is on average 5 m higher on the western than its eastern sides. Earlier studies based on results from shallow trenching (e.g., Smith et al., 2014) suggested a possibility for a post-glacial fault associated with the scarp. **(b)** LiDAR data (no shading) showing the location of the scarp relative to where the geophysical data presented in this study were acquired. Seismic data were only acquired along profile 1. Our DGPS-elevation measurements along profile 1 are shown as an inset figure in **(b)**.

SED
7, 2833–2874, 2015

Figure 4. (a) Field photos showing **(a)** the seismic data acquisition using combined wireless (24-fixed, 20 m spacing) and cabled (92-MEMs-based streamer and planted, 2–4 m spacing) seismic recorders and Bobcat-mounted drop hammer as the seismic source. **(b)** Gravity (128 points were measured) and geodetic surveying. **(c)** RMT data acquisition (10 m spacing along profiles 1 and 2). **(d)** Total-field magnetic surveying. The geophysical data acquisition took totally 6 days in two separate field campaigns during October 2014. The Bollnäs scarp and its apparent displacement is visible in (**a**; see the half arrows).

SED
7, 2833–2874, 2015

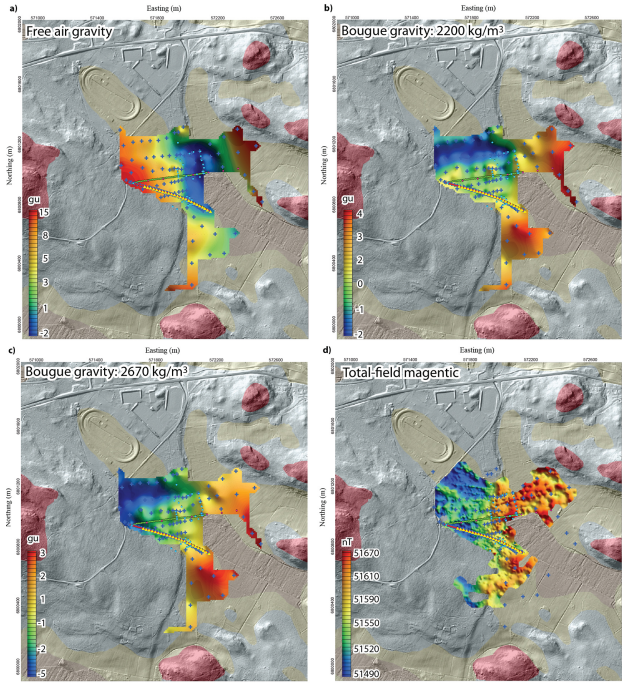

Figure 5. (a) Free-air gravity map, **(b)** Bouguer gravity map (corrected using a density of 2200 kg m^{-3}) accounting for the sediments forming the topography, **(c)** Bouguer gravity map obtained by a standard topographic correction of 2670 kg m^{-3} and **(d)** total-field magnetic map of the study area. A clear indication of gravity and magnetic high on the eastern side of the scarp is noticeable. Magnetic data clearly suggest a lineament about 50–60 m west of the scarp. Gravity data are shown as the gravity unit (gu).

SED
7, 2833–2874, 2015

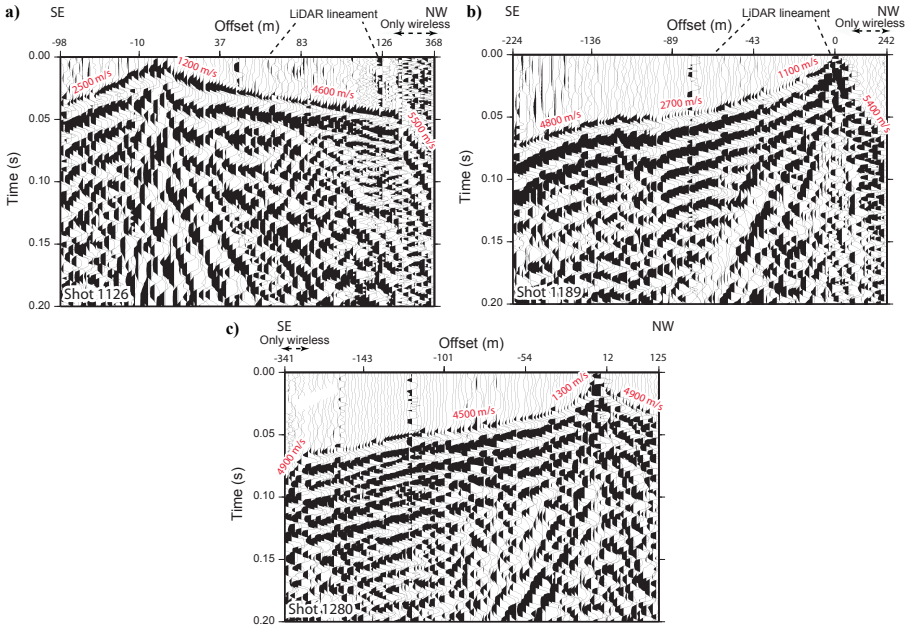

Figure 6. Example shot gathers from **(a)** eastern, **(b)** central and **(c)** western parts of profile 1 (also scarp) showing the quality of the seismic data particularly first breaks and an indication of deeper bedrock in the western side of the scarp. The central shot suggests an apparent low velocity zone (2700 m s^{-1}). The far-offset data are from wireless recorders that are about 20 m apart.

SED
7, 2833–2874, 2015

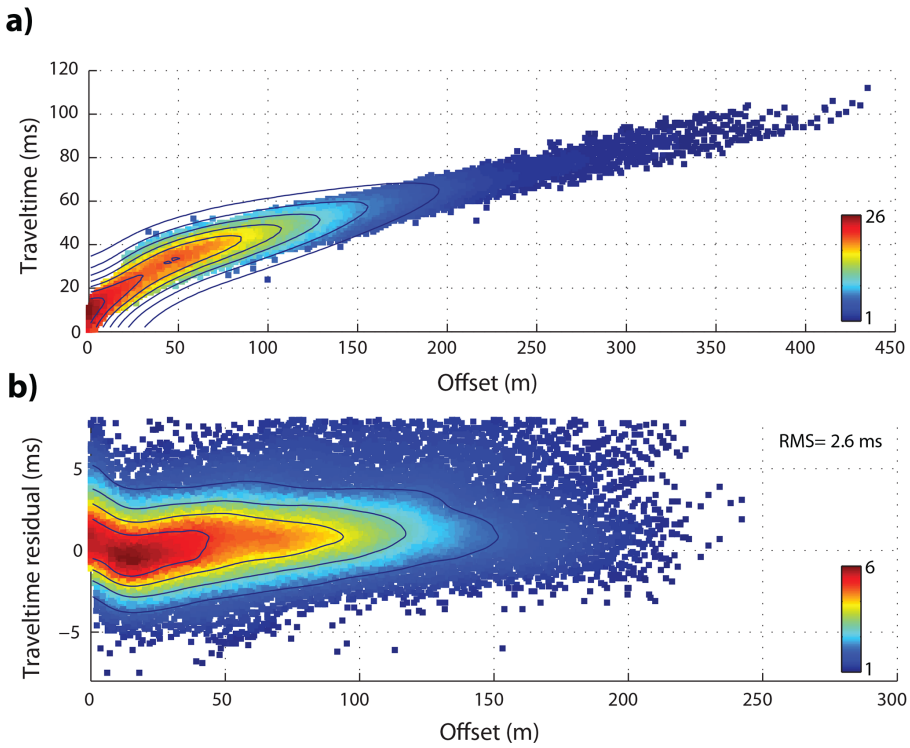

Figure 7. (a) All first break picks as a function of offset (color-coded and contoured base on the data density). **(b)** The travel time residuals (observed minus calculated traveltimes) as a function of offset for all the receiver locations obtained in the last inversion iteration. An RMS of 2.6 ms was obtained. Note that high RMS picks were discarded during the inversion resulting in smaller offsets in the final inversion than those that were picked.

SED
7, 2833–2874, 2015

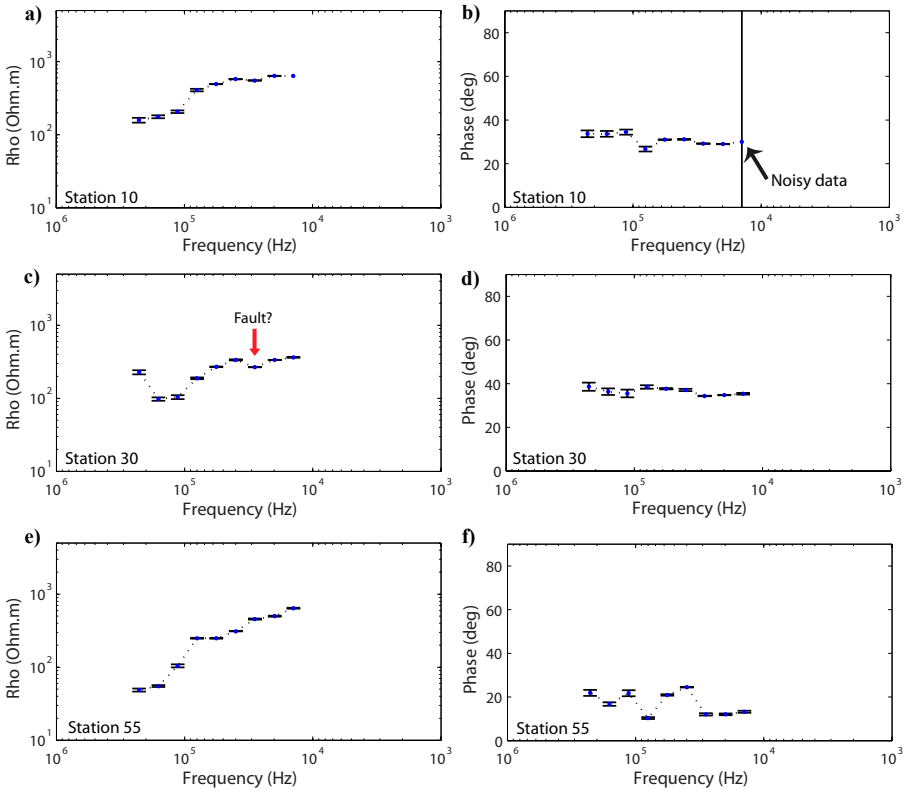

Figure 8. Example raw phase and resistivity data from **(a–b)** eastern, **(c–d)** central and **(e–f)** western parts of the scarp (profile 1) showing the quality of the data but also potentially a high-conductivity zone already inferable from the apparent resistivity data in the central part of profile 1 (see the red arrow).

SED
7, 2833–2874, 2015

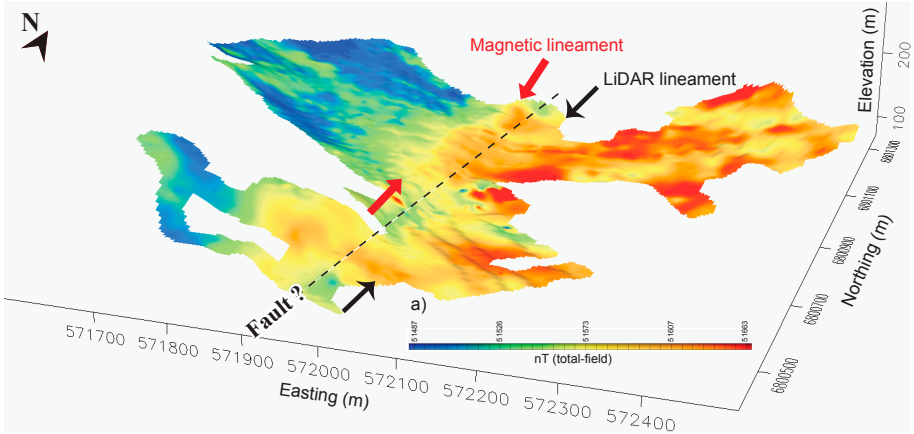

Figure 9. Total-field magnetic data gridded and projected onto the LiDAR data (Fig. 3) clearly suggesting a magnetic lineament about 50–60 m west of the scarp separating a magnetic high (~ 200 nT) region from a rather low one. We attribute this to a basement high in the eastern side of the scarp somewhere at half way between the magnetic lineament and the LiDAR lineament (see the black dashed line). This is likely the actual location of a basement fault forming the Bollnäs scarp (see also Fig. 2b).

SED
7, 2833–2874, 2015

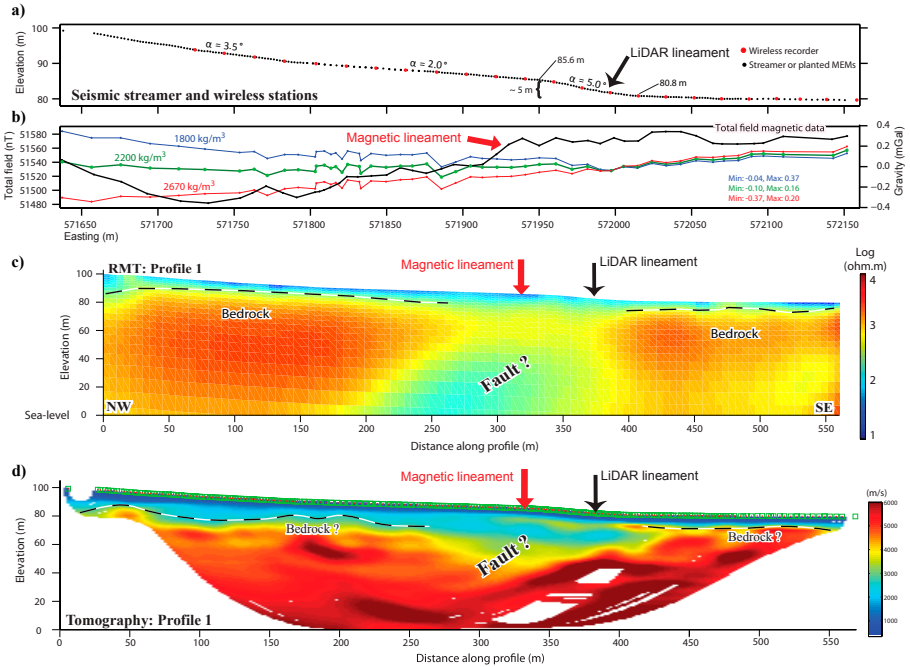

Figure 10. A compilation of **(a)** DGSP geodetic surveying of the seismic stations showing the general topography in the study area, **(b)** magnetic and gravity data (various Bouguer corrections), **(c)** the RMT results and **(d)** P-wave first-arrival tomography results along profile 1 (Fig. 3). Note how consistently all these suggest a weak zone (low-velocity and high-conductivity), attributed to a fault in the bedrock, slightly west of the scarp. Bedrock is shallower in the eastern side of the scarp but no estimation of possible fault throw can be given due to the larger thickness of sediments on the western side of the scarp.

SED
7, 2833–2874, 2015

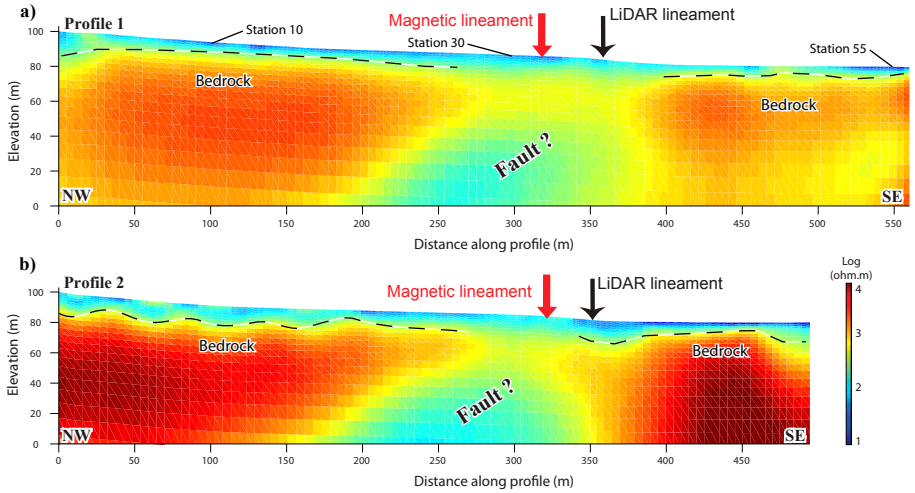

Figure 11. RMT results along **(a)** profile 1 and **(b)** profile 2 consistently showing a clear evidence of a conductivity structure west of the scarp and in the bedrock. They also suggest that the bedrock is likely shallower on the eastern side of the scarp than its western side. We attribute the conductive zone to highly fractured and water-bearing bedrock and possibly an indication of a post-glacial fault. RMT data for stations 10, 30 and 55 are shown in Fig. 8.

SED
7, 2833–2874, 2015

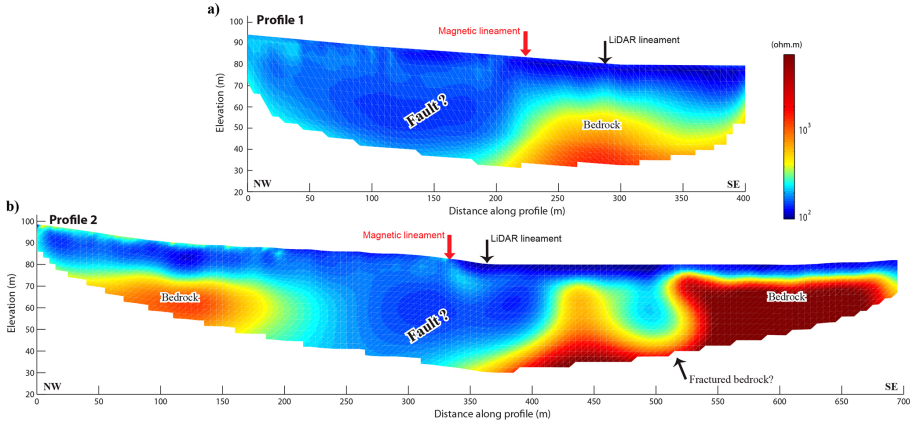

Figure 12. ERT results along **(a)** profile 1 and **(b)** profile 2 consistently showing a clear evidence of a conductivity structure west of the scarp. They also suggest that the bedrock is shallower on the eastern side of the scarp than its western side consistent with the magnetic (Fig. 9), RMT (Fig. 11) and the seismic results (Fig. 10).

SED
7, 2833–2874, 2015

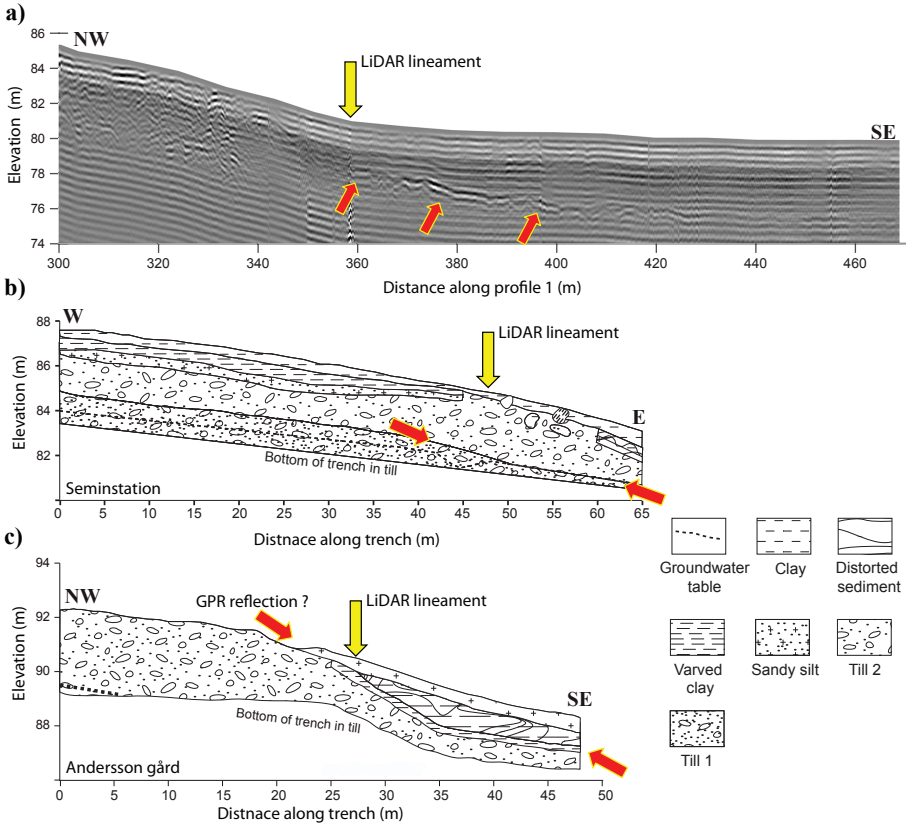

Figure 13. (a) Example of GPR profile recorded across the scarp exhibiting a gently dipping reflection immediately east of the scarp. This is interpreted as the base of the till as **(b)** observed in one of the trenches (Seminstation in Fig. 3b) reported by Smith et al. (2014). It can also suggest a fault on its western-end side because the reflection disappears there. **(c)** The Andresson gård trench extends to the eastern side of the scarp hence is also used for a better comparison here.

SED
7, 2833–2874, 2015

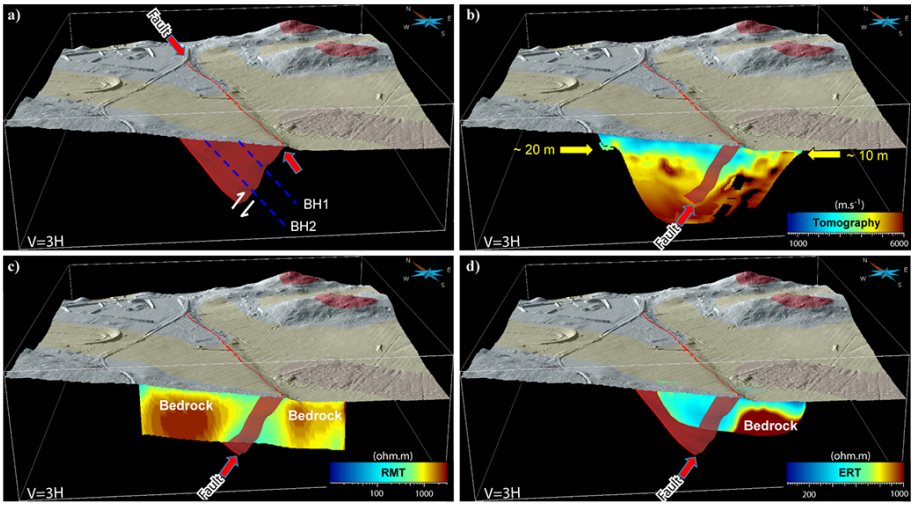

Figure 14. 3-D visualization of the geophysical results along profile 1. **(a)** Surface geology projected onto the LiDAR data with a hypothetical shape of the Bollnäs fault plane (assumed to be reverse) generated using the magnetic lineament observed in our own data, **(b)** travel time tomography, **(c)** RMT, and **(d)** ERT models. Future plans should aim at drilling (e.g., BH1 and BH2) the weak zone that is interpreted to be a deformation zone hosting the Bollnäs post-glacial fault and defining the bedrock level along profile 1. A better estimation of the throw may be then estimated and downhole logging would be conducted to verify the geophysical results presented here.

SED
7, 2833–2874, 2015

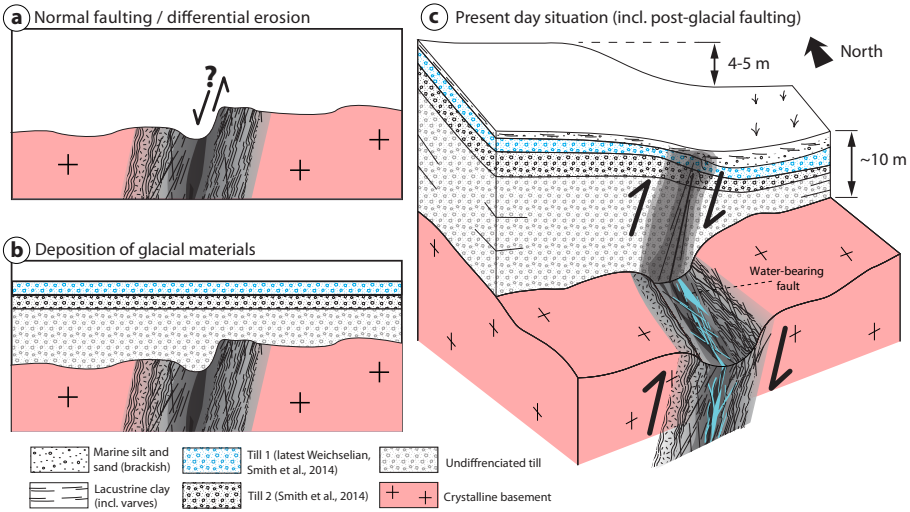

Figure 15. Schematic scenarios explaining the Bollnäs scarp and our interpretation of the geophysical results. **(a)** A damage zone inherited from brittle deformation events overprints earlier ductile deformation structures (Svecokarelian basement). **(b)** A varying thickness of till sequence covers the basement that is thought to be deeper on the western side of the scarp than on the eastern side prior to the Weichsel glaciation. **(c)** The scarp is related to a recent (10 200 BP; Smith et al., 2014) reversed fault in the basement that is water bearing (in blue). Top basement shows little to no obvious offset. Deformation patterns affecting the glacial deposits (e.g., water-escaped features) reported in Smith et al. (2014) are not detailed here.

SED
7, 2833–2874, 2015